





## Dissolution regimes of a horizontal channel in a gravity field

Wei Guo , Ran Hu \*, Chen-Xing Zhou , Zhibing Yang, and Yi-Feng Chen  
*State Key Laboratory of Water Resources Engineering and Management, and Key Laboratory of Rock Mechanics in Hydraulic Structural Engineering of the Ministry of Education, Wuhan University, Wuhan 430072, China*

 (Received 30 March 2023; accepted 16 November 2023; published 11 December 2023)

Buoyancy-driven dissolution of the solid phase is common in natural processes and subsurface applications, such as geomorphology, solution mining, and geological CO<sub>2</sub> storage. When an external horizontal flow is imposed, the dissolution dynamics are controlled by the interplay between buoyancy-driven and forced convections. The reshaping of the solid surface due to this interplay is not well understood. Here, we fabricate a soluble microfluidic chip with a horizontal channel to investigate the pore-scale dissolution dynamics in a gravity field. We observe that the wave number and the surface roughness factor of the upper solid-liquid interface initially increases with the flow rate (Péclet number  $Pe$ ) and then decreases, indicating two dissolution regimes, namely, Regimes I and II. Microparticle-image-velocimetry-based imaging reveals that the eddy evolution occurring in the flow-dissolution system controls the local dissolution rate and the geometry evolution of the solid-liquid interface. Through the quantification of the eddies (or troughs) for the whole channel, the number of the eddies increases with  $Pe$  in Regime I and decreases with  $Pe$  in Regime II, indicating that the buoyancy-driven convection is enhanced in Regime I and suppressed in Regime II by the forced convection. Finally, by performing a theoretical analysis of the density gradient, we obtain a scaled critical aperture, i.e., the critical aperture normalized by a characteristic length, for the onset of unstable dissolution of the solid-liquid interface. Such a scaled critical aperture is constant for both dissolution regimes. In this paper, we elucidate the crucial role of eddies in the flow-dissolution system in a gravity field. Moreover, we improve our understanding of the interplay between buoyancy-driven and forced convections in etching the solid surface.

DOI: [10.1103/PhysRevFluids.8.123902](https://doi.org/10.1103/PhysRevFluids.8.123902)

### I. INTRODUCTION

The occurrence of buoyancy-driven dissolution in permeable media, especially if halite or carbonate minerals are present, may significantly affect the groundwater chemistry and the hydrodynamic behavior of the underground formations. This issue is closely related to many subsurface applications, such as the origin of karst systems [1,2], dam stability [3], solution mining [4], and geological CO<sub>2</sub> storage or leakage [5–10]. The buoyancy effect on solutal dissolution, that is, the dissolution of a solute from one liquid to a homogeneous liquid mixture, has been extensively studied [5,6,11–21]. When a layer of saturated solution contacts an aqueous solution from the top, the solute dissolves into the surrounding liquid near the surface and gradually generates a boundary layer with high concentration. This concentration boundary layer (CBL) is denser than the surrounding less concentrated fluid. Due to gravity, buoyancy-driven convection in the form of dense plumes then appears. The strength of the buoyancy-driven convection is determined by the

---

\*Corresponding author: [whuran@whu.edu.cn](mailto:whuran@whu.edu.cn)

Rayleigh number  $Ra$ . As  $Ra$  increases, the onset time of convection is reported to decrease, and the dissolution rate was shown to increase [22,23]. Consequently, the CBL tends to deform greatly with more and narrower plumes [17,24]. These studies focused on the convective dissolution occurring in a two-fluid system, in which the dissolution of the solid phase is not considered.

For the solid-liquid system in a gravity field, the evolution of the solid-liquid interface is controlled by buoyancy-driven convection. Without external-flowing conditions, the solid-liquid interface gradually becomes unstable in buoyancy-driven dissolution [13,14,25–27]. Cohen *et al.* [13,26] reported that scallops would form on the wall of a dissolving caramel block because of buoyancy-driven convection. Through visualized experiments, Davies Wykes *et al.* [14] showed that, in a gravity field, a flat boundary dissolving from its lower surface tends to become rough and pitted. These researches indicated that the buoyancy-driven convection would reshape the solid surface by inducing a heterogeneous concentration near the solid-liquid interface.

When an external horizontal flow is imposed, the dissolution dynamics are controlled by the interplay between buoyancy-driven and forced convections [22,28–37]. In a pioneer work, Dijk and Berkowitz [33] reported that, when the two-dimensional (2D) rough fracture in the natural halite sample is oriented horizontally, the upper fracture wall dissolves more rapidly than the lower one. Through pore-scale experiments and simulation, Hu *et al.* [35] also found that the buoyancy-driven convection would break the symmetry of dissolution on the upper and lower surfaces for a horizontal channel. Using this concept, they propose three dissolution regimes to quantify the gravitational effects on the dissolution regimes and permeability evolution for three-dimensional (3D) rough fractures. Recently, Michel-Meyer *et al.* [32] claimed that forced convection suppresses small-wavelength fluctuations by enhancing dispersion among plumes, leading to the decrease of the wave number, and the dissolution rate for all flow rates showed no difference. Similar results were also reported by Tsinober *et al.* [31]. However, another group of studies reported that the increase in the horizontal flow would result in a decrease in the overall dissolution rate [22,29,30]. This suggests that the interplay between forced and buoyancy-driven convections controlling the dissolution processes is much more complicated, which may depend on several factors, such as the eddy developments at the pore scale [38,39].

In this paper, we aim to investigate how the interplay between buoyancy-driven and forced convections affects solid-liquid surface dissolution at the pore scale. We developed a microparticle-image-velocimetry (micro-PIV)-based flow-visualization system that enables us to capture the evolution of the solid-liquid interface and the associated flow velocity field in a horizontal microfluidic channel (Sec. II). Through observation and quantification, we identify two dissolution regimes (Sec. III), and we find that the flow-dissolution feedback loop controls local surface evolution and mass transport. Additionally, we present a scaled, regime-independent critical aperture for the onset of the solid-liquid interfacial evolution. In this paper, we provide a better understanding of dissolution dynamics in a horizontal geometry under gravity, which has important implications for a wide range of applications in fields such as subsurface hydrology, geophysics, chemical engineering, and materials science.

## II. MATERIALS AND METHODS

### A. Fabrication of microfluidic soluble channels

The fabrication of a microfluidic soluble chip consists of three procedures (Fig. 1). First, a single channel with smooth surfaces is etched on a salt crystal (NaCl) chip (15 mm in length, 10 mm in width, 0.8 mm in thickness) using laser etching technology [Fig. 1(a)] with the resolution of 20  $\mu\text{m}$ . The geometries for all channels used can be assumed to have identical initial conditions for the flow-through dissolution experiments. In addition, we polish the crystal slices as thin as possible (0.8 mm) to ensure the aperture along the spanwise direction is homogeneous. The initial mean aperture and the initial pore volume (PV) of the channel are, respectively,  $\langle b_0 \rangle = 0.5$  mm and  $V_0 = 6.0$   $\mu\text{L}$ . Second, we fix the etched NaCl crystal into a slot carved in the polydimethylsiloxane

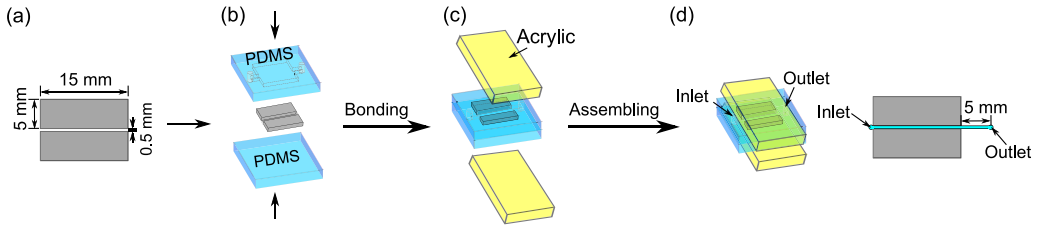


FIG. 1. Fabrication of soluble microfluidic channels. (a) A NaCl crystal chip is etched by the laser etching technology according to a horizontal smooth channel pattern with the initial aperture being 0.5 mm. (b) The NaCl crystal chip is fixed into the slot of a polydimethylsiloxane (PDMS) layer and is bonded by another smooth PDMS plate using a plasma cleaner (Harrick Plasma, PDC-002). (c) Two transparent acrylic bars are finally assembled to fix the chip firmly. (d) A microfluidic model with a soluble horizontal channel is created.

(PDMS) layer [Fig. 1(b)], and bond it to a smooth PDMS plate using a plasma cleaner (PDC-002, Harrick Plasma, USA). The generation of the upper carved PDMS layer has three steps: (1) using laser etching technology to print the designed geometry on the acrylic plate master. The inner size of the rectangular slot is designed the same as the size of the NaCl crystal chip, (2) pouring PDMS onto the acrylic plate master and heating it at 80 °C for 2 h, and (3) cutting the cured PDMS off the master to obtain the carved PDMS layer. The inlet is located close to the left end of the channel, and the outlet is set 5 mm away from the right end of the channel [Figs. 1(d) and 2(c)]. The inlet and outlet of the chip are located at both ends of the channel. Third, two transparent acrylic bars are finally assembled to fix the chip firmly [Fig. 1(c)]. The microfluidic model can be regarded as a quasi-2D chip with etched NaCl crystals embedded inside the chamber, which allows us to visualize and capture the quasi-2D surface variation of the channels during the dissolution experiments [Figs. 1(d) and 2(c)].

## B. Experimental procedures

We perform a flow-through dissolution experiment in horizontal channels to study the interplay between buoyancy-driven (due to gravity) and forced (due to externally imposed flow rate) convections using a micro-PIV system (Figs. 2 and 3). We first fix the microfluidic chip, as shown in Fig. 2, ensuring that the direction of fluid flow is perpendicular to the direction of gravitational acceleration. The initial smooth channel is in the center of the field of view (FOV) of the camera, and its left end is aligned with the edge of the FOV [Fig. 4(a)]. To conduct a flow-through dissolution experiment, we inject the saturated brine solution ( $C_{\text{eq}} = 312 \text{ g/L}$ , 25 °C) into the microfluidic channel through syringe pump A (Harvard Ph.D. Apparatus) at a slow flow rate of 1  $\mu\text{L}/\text{min}$ . This procedure lasts until six PVs of saturated brine are injected into the channel to ensure that the flow domain is filled with saturated brine and no air is trapped in the channel. Then we switch on syringe pump B (Harvard Ph.D. Apparatus) to inject the deionized (DI) water continuously into the microfluidic chip with the flow rate  $Q$  ranging from 9.73 to 194.12  $\mu\text{L}/\text{min}$  (Table I) until the channels have been completely dissolved. The injected DI water is dyed with Erioglaucine disodium salt (Macklin, E808678) to increase the difference of signal intensity between the liquid and the NaCl crystal. The dissolution shown by the recession of the solid-liquid interface begins after the freshwater flushes the saturated brine away from the channel (Appendix B). Here, we only focus on the dissolution process after the saturated brine has been displaced. Therefore, the time of  $t = 0$  corresponds to the beginning of the solid dissolution (after the displacement of saturated brine by freshwater), as indicated in Fig. 5. Given that the inflowing fluid is pure water, the NaCl crystal continually dissolves into the water flow. The dissolution process, including the flow velocity field and the fluid-solid interface, is visualized by the micro-PIV system (LaVision) [40,41]. A charge-coupled device (CCD) camera with a 6 megapixel ( $2752 \times 2200$  pixel array) sensor and a pixel size of 4.5  $\mu\text{m}$  is coupled with the stereoscopic microscope, installed in front of the chip to provide

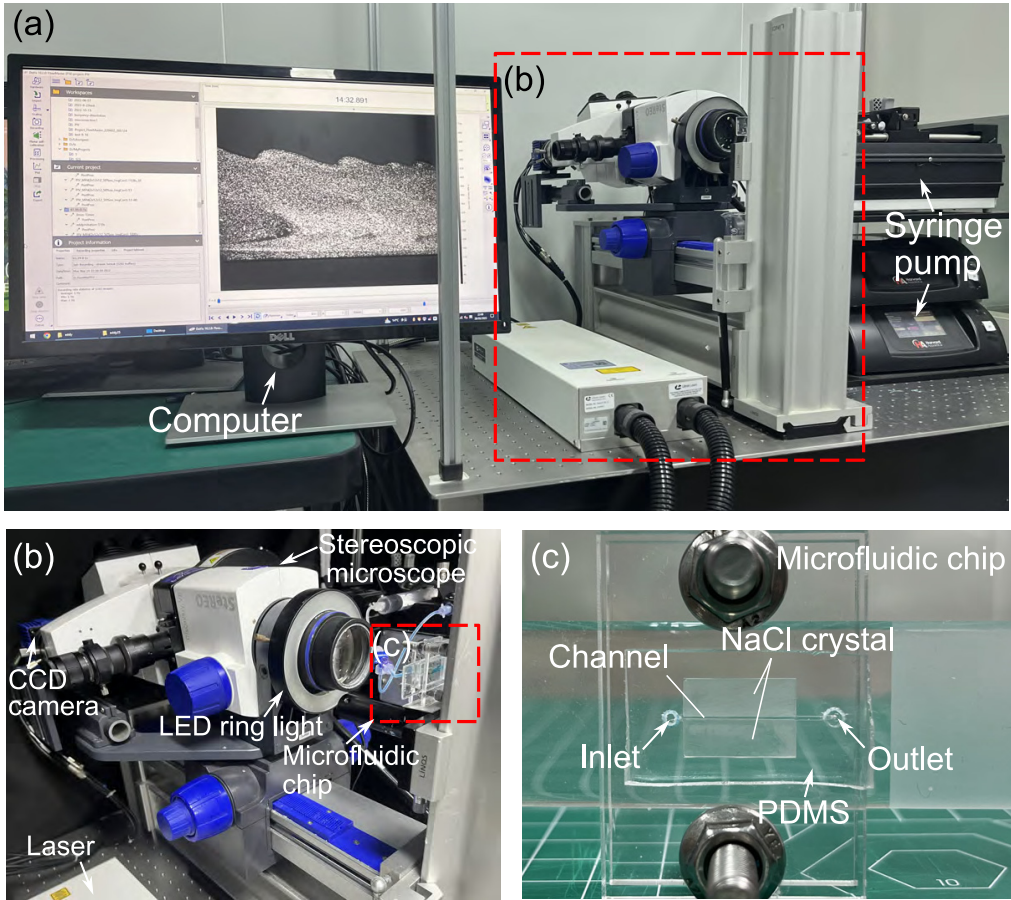


FIG. 2. The microparticle-image-velocimetry (micro-PIV)-based flow-visualization system for imaging the dissolution of a horizontal channel in a gravity field. (a) Micro-PIV system, (b) charge-coupled device (CCD) camera coupled with the stereoscopic microscope, and (c) soluble microfluidic chip.

real-time recording of the dissolution process at the frequency ranging from 0.2 to 1 frames/s. The stereoscopic microscope can result in a magnification ranging from  $1 \times$  to  $8 \times$ . A LED parallel light is installed in front of the stereoscopic microscope to light up the flow domain [42]. The system allows capturing the quasi-2D surface variation of the channels during the dissolution.

To perform a micro-PIV experiment, a dual-pulsed Evergreen Nd : YAG laser with a maximum energy of 30 mJ/pulse is used to form a  $\sim 0.8$ -mm-thick laser sheet to illuminate the tracer particles in the flow domain. For the micro-PIV experiment, we replace the LED light with a laser. Fluorescent particles  $\sim 5 \mu\text{m}$  in diameter are included in the fluid flow as tracers, and their fluoresced light is recorded through a long-pass 580 nm filter. We keep the mass concentration of fluorescent particles at  $\sim 1 \text{ mg/mL}$  in DI water to provide sufficient particle number density in the fluid such that each PIV interrogation window contains a sufficient number of particles to obtain a reliable velocity measurement (5–10 particles per  $16 \times 16$  pixel interrogation window, see Movie S2 in the Supplemental Material [43]) [41]. The computer controls the CCD camera and the laser to work synchronously, further processes the captured images, and calculates the flow field (see more details in Appendix B).

The dissolution process studied in this paper is controlled by the interplay between the forced convection, as measured by Péclet number  $Pe = v\langle b_0 \rangle / D_m$ , and the buoyancy effect of hydrody-

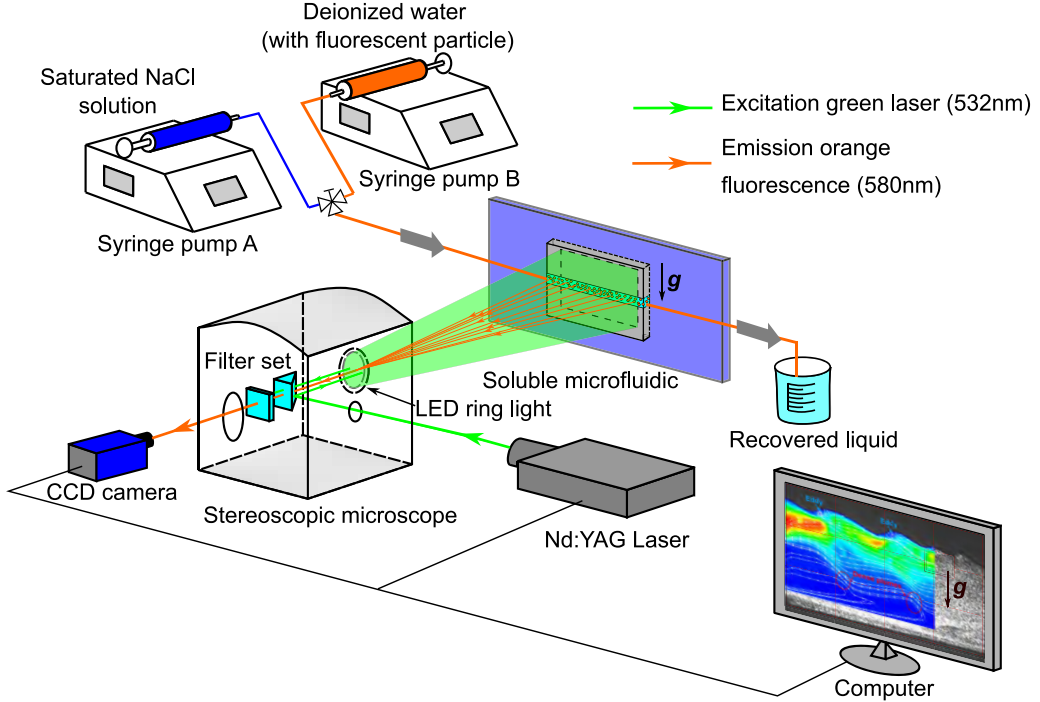


FIG. 3. Experimental setup of microparticle image velocimetry (micro-PIV). The deionized (DI) water mixed with fluorescent particles with a diameter of  $\sim 5 \mu\text{m}$  is injected into the channel by syringe pump B after the initial saturation of the channel. Since fluorescent particles can be excited by the green laser ( $\sim 532 \text{ nm}$ ), the movement of particles in channels can be captured by the charge-coupled device (CCD) camera, and the flow velocity field can be calculated by analysis software (DaVis 10.0). The entire experimental system is maintained at room temperature ( $25 \pm 0.5^\circ\text{C}$ ) with an air conditioner.

dynamic instabilities, that is, the buoyancy-driven convection, characterized by the Rayleigh number  $\text{Ra} = \Delta\rho g K \langle b_0 \rangle / (\mu_f D_m)$ . The flow velocity  $v$  is defined as  $v = Q / (d_0 \langle b_0 \rangle)$ , where  $Q$  is the constant volume flow rate imposed by syringe pump,  $d_0$  is the thickness of the channel with  $d_0 = 0.8 \text{ mm}$ ,  $\langle b_0 \rangle$  is the initial mean aperture of the channel,  $D_m$  is the molecular diffusion coefficient,  $K$  is the permeability  $K = \langle b_0 \rangle^2 / 12$ ,  $\Delta\rho$  is the density difference between pure water and the saturated brine solution,  $g$  is the gravitational acceleration, and  $\mu_f$  is the dynamic viscosity. Note that  $\text{Pe}$  and  $\text{Ra}$  are defined at the inlet  $x = 0$  and  $t = 0$ , corresponding to the initial geometry of the microfluidic channel. During the dissolution, the aperture at  $x = 0$  increases, and the average flow velocity  $Q / (d_0 \langle b_0 \rangle)$  decreases. Thus, the Péclet number defined at  $x = 0$  and  $t = 0$  would decrease during flooding. The conditions for all experiments are listed in Table I.

### C. Image processing for solid-fluid interface and flow velocity field

Images acquired during dissolution are processed to allow for a qualitative and quantitative study. Given the significant difference in signal intensity between dyed water and NaCl crystal, the evolution of the solid-fluid interface can be captured accurately by the following step. First, a raw gray image [Fig. 4(b)] is converted to a binary image via the function `IM2BW` in MATLAB. The images are then filtered using the function `BWAREAOPEN` to limit noise appearing during acquisition. Once the binary image [Fig. 4(c)] is obtained, the raw data can be transformed into segmented images with two phases, and the corresponding solid-fluid interface can be easily captured. The FOV of the visualized experiments is  $\sim 12.5 \times 9.9 \text{ mm}^2$  ( $L \times W$ ), determined by the resolution and

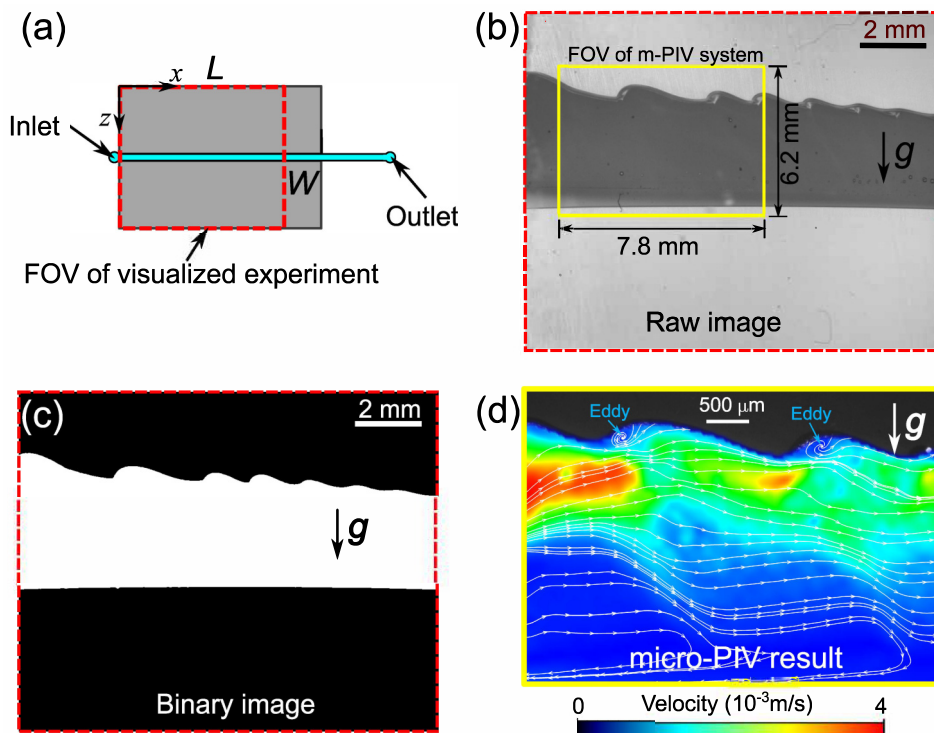


FIG. 4. Image processing and the characterization of the flow velocity field. (a) The location of the field of view (FOV) of the visualized experiment. The red dashed box denotes the FOV of visualized experiments. (b) The raw grayscale image captured by the charge-coupled device (CCD) camera. The yellow box denotes the FOV of microparticle-image-velocimetry (micro-PIV) experiments. (c) The processed binary image. (d) The result of the local flow velocity field.

pixel size of the CCD camera [Fig. 4(a)]. For the micro-PIV experiments, the captured raw particle image can be processed and calculated with LaVision DaVis 10.0 software using a sequential cross-correlation algorithm with a final interrogation window size of 256 pixels with 50% overlap, resulting in a vector field resolution of  $\sim 0.12$  mm and a vector grid spacing of  $\sim 0.06$  mm. The FOV of the micro-PIV setup is  $\sim 7.8 \times 6.2$  mm<sup>2</sup>. The calculated local flow velocity field postprocessed by the software TECPLOT is shown in Fig. 4(d). Note that the thickness of the channel in this paper (800  $\mu$ m) is less than the wavelength of convective plumes driven by buoyancy-driven dissolution in the salt-water system ( $\sim 1$  mm) [11,13], suggesting that the spanwise of the channel would not become rough due to buoyancy-driven dissolution. Thus, the flow dynamics in this microfluidic channel can be approximated as 2D.

### III. RESULTS AND DISCUSSION

#### A. Observation of dissolution regimes

To investigate how the surface geometry evolves during dissolution in a gravity field, we first present the morphologies of the channel surface from the initial state ( $\langle b \rangle = \langle b_0 \rangle$ ) to later states ( $\langle b \rangle = 3\langle b_0 \rangle$  and  $6\langle b_0 \rangle$ ) under various flow conditions ( $Pe = 126$ – $2512$ ), as shown in Fig. 6. We observe that most of the NaCl crystal dissolution occurs on the upper surface, while the geometry of the lower surface stays nearly unchanged. This is because the injected fresh water has a lower density, and it preferentially flows near the upper surface, which significantly enhances

TABLE I. Summary of flow-through dissolution experiments in a gravity field. The chosen parameters for saturated brine solution are  $D_m = 1.61 \times 10^{-9} \text{ m}^2 \text{ s}^{-1}$ ,  $\mu_f = 1.99 \times 10^{-3} \text{ Pa} \cdot \text{s}$  (saturated concentration),  $\rho_m = 1200 \text{ kg/m}^3$ ,  $\Delta\rho = 200 \text{ kg/m}^3$ , and  $C_m = 312 \text{ g/L}$  [11]. The permeability of the channel is calculated as  $K = 2.08 \times 10^{-8} \text{ m}^2$ .  $Q$  is the injection flow rate by a syringe pump.  $v$  is the initial average velocity calculated by the injection flow rate divided by the initial channel cross-sectional area.  $x_c$  is the horizontal distance from the leftmost end of the channel to the first observable trough position.  $b_c$  is the critical aperture at  $x = x_c$  when the first observable trough is generated.  $\Delta X (t_{\text{end}})$  is the horizontal distance from the beginning of the first trough to the rightmost side of the FOV.

Exp. #	$Q$ ( $\mu\text{L}/\text{min}$ )	$v$ (m/s)	$\text{Pe} = v$ $\langle b_0 \rangle / D_m$	$\text{Ra} = \Delta\rho g K$ $\langle b_0 \rangle / (\mu_f D_m)$	$x_c$ (mm)	$b_c$ (mm)	$\Delta X (t_{\text{end}})$ (mm)
1	9.73	$1.01 \times 10^{-4}$	126	6372	2.60	3.23	10.14
2	9.73	$1.01 \times 10^{-4}$	126	6372	/ <sup>a</sup>	/	/
3	12.25	$1.28 \times 10^{-4}$	158	6372	2.13	3.33	10.65
4	12.25	$1.28 \times 10^{-4}$	158	6372	2.23	2.93	10.40
5	15.42	$1.61 \times 10^{-4}$	200	6372	3.20	2.70	9.69
6	15.42	$1.61 \times 10^{-4}$	200	6372	2.69	2.87	11.00
7	19.41	$2.02 \times 10^{-4}$	251	6372	2.55	2.72	10.99
8	25.03	$2.60 \times 10^{-4}$	324	6372	3.50	2.68	11.00
9	25.03	$2.60 \times 10^{-4}$	324	6372	2.98	2.63	10.62
10	30.91	$3.22 \times 10^{-4}$	400	6372	2.20	2.49	10.83
11	30.91	$3.22 \times 10^{-4}$	400	6372	1.90	2.80	10.96
12	38.73	$4.03 \times 10^{-4}$	501	6372	4.00	2.52	8.88
13	38.73	$4.03 \times 10^{-4}$	501	6372	4.30	2.08	8.50
14	43.46	$4.53 \times 10^{-4}$	562	6372	2.50	2.10	11.36
15	43.46	$4.53 \times 10^{-4}$	562	6372	3.16	2.07	10.66
16	48.76	$5.08 \times 10^{-4}$	631	6372	2.85	2.02	10.89
17	48.76	$5.08 \times 10^{-4}$	631	6372	2.68	1.98	10.74
18	61.39	$6.39 \times 10^{-4}$	794	6372	3.61	2.14	10.70
19	61.39	$6.39 \times 10^{-4}$	794	6372	2.72	1.86	10.20
20	77.28	$8.05 \times 10^{-4}$	1000	6372	2.94	2.14	9.38
21	77.28	$8.05 \times 10^{-4}$	1000	6372	3.65	1.82	10.58
22	97.29	$1.01 \times 10^{-3}$	1259	6372	3.64	2.02	10.10
23	97.29	$1.01 \times 10^{-3}$	1259	6372	3.76	2.05	9.92
24	122.48	$1.28 \times 10^{-3}$	1585	6372	4.00	2.12	10.07
25	122.48	$1.28 \times 10^{-3}$	1585	6372	3.44	1.97	10.20
26	154.19	$1.61 \times 10^{-3}$	1995	6372	4.50	2.00	9.53
27	194.12	$2.02 \times 10^{-3}$	2512	6372	5.50	2.11	8.61

<sup>a</sup>Trough is not observed in exp. #2.

the dissolution of NaCl crystal on this surface. The lower surface, however, dissolves little because the solution near this surface is hardly renewed. The underlying mechanism of this difference on the upper and lower surfaces has been revealed by PIV measurement (see more details in Appendix C). Moreover, we observe rougher upper solid-liquid interfaces as the channel expands; that is, many troughs gradually appear along the upper surface from inlet to outlet. According to the different upper dissolution geometries for various Pe, two typical dissolution regimes are observed. For Regime I (Pe = 126–631), owing to the slow transport of dissolved solute (salt) under these low Pe conditions, the upper NaCl crystal dissolves more near the inlet but little near the outlet. This indicates that the concentration of fluid near the upper surface gradually increases along the flow direction. Thus, it leads to a converging geometry, which has been reported extensively in previous works [34,42,44]. Additionally, as Pe increases from 126 to 631, more troughs are generated at the upper surface. However, the number of troughs in Regime II is observed to decrease as Pe

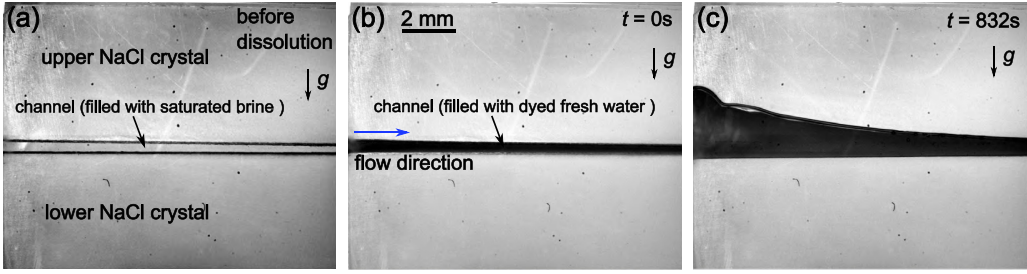


FIG. 5. The definition of the initiation of dissolution ( $Pe = 126$ ). (a) The channel filled with saturated NaCl solution before dissolution. (b) The beginning of dissolution ( $t = 0$  s). It is defined as the beginning of the recession of channel interfaces, which can be captured with the high-frame-rate charge-coupled device (CCD) camera. Note that the channel has nearly been filled with the dyed fresh water at this time. (c) The dissolution morphology of channel at  $t = 832$  s.

increases from 794 to 2512 (Fig. 6). The upper solid-liquid interface seems to become smoother as  $Pe$  increases in this regime. This dissolution-induced rough surface is under the control of Rayleigh-Taylor instability, and it has been investigated in depth under a no-external-flowing condition [11,13,17,33,45]. Here, we focus on the evolution of dissolution-induced instability in a gravity field under forced convection conditions.

To quantify how the interplay between buoyancy-driven and forced convections controls the dissolution, we characterize the dissolution morphologies of the upper solid surface using the average wave number  $\kappa$ , the average amplitude  $\sigma$ , and the surface roughness factor (SRF) at  $t = t_{\text{end}}$  (Fig. 7). Here,  $\kappa$  and  $\lambda$  are defined as  $\kappa = 2\pi/\lambda$  and  $\lambda = \Delta X(t_{\text{end}})/N_f$  [32], where  $\Delta X(t_{\text{end}})$  is the horizontal length of the analyzed area from the beginning of the first trough to the rightmost side of the FOV [Fig. 7(b), as listed in Table I],  $N_f$  is the number of the peaks identified by FINDPEAKS

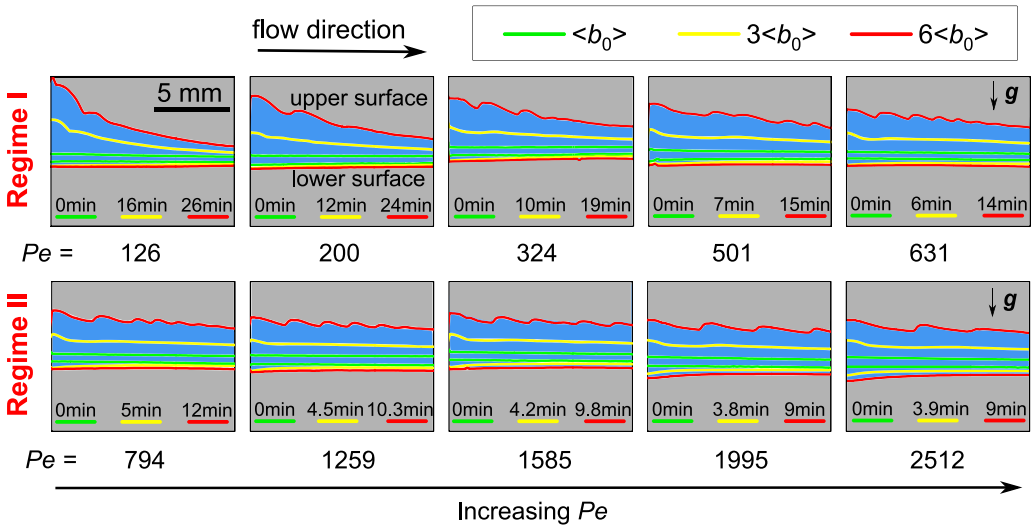


FIG. 6. Observation of dissolution regimes of the microfluidic channels in a gravity field. Evolution of channel surface morphology with  $Pe$  increasing from 126 to 2512. The typical morphologies of channel surfaces are presented via the lines with different colors, corresponding to  $\langle b \rangle = \langle b \rangle$ ,  $3\langle b \rangle$ , and  $6\langle b \rangle$ . The corresponding times elapsed after dissolution are also denoted.



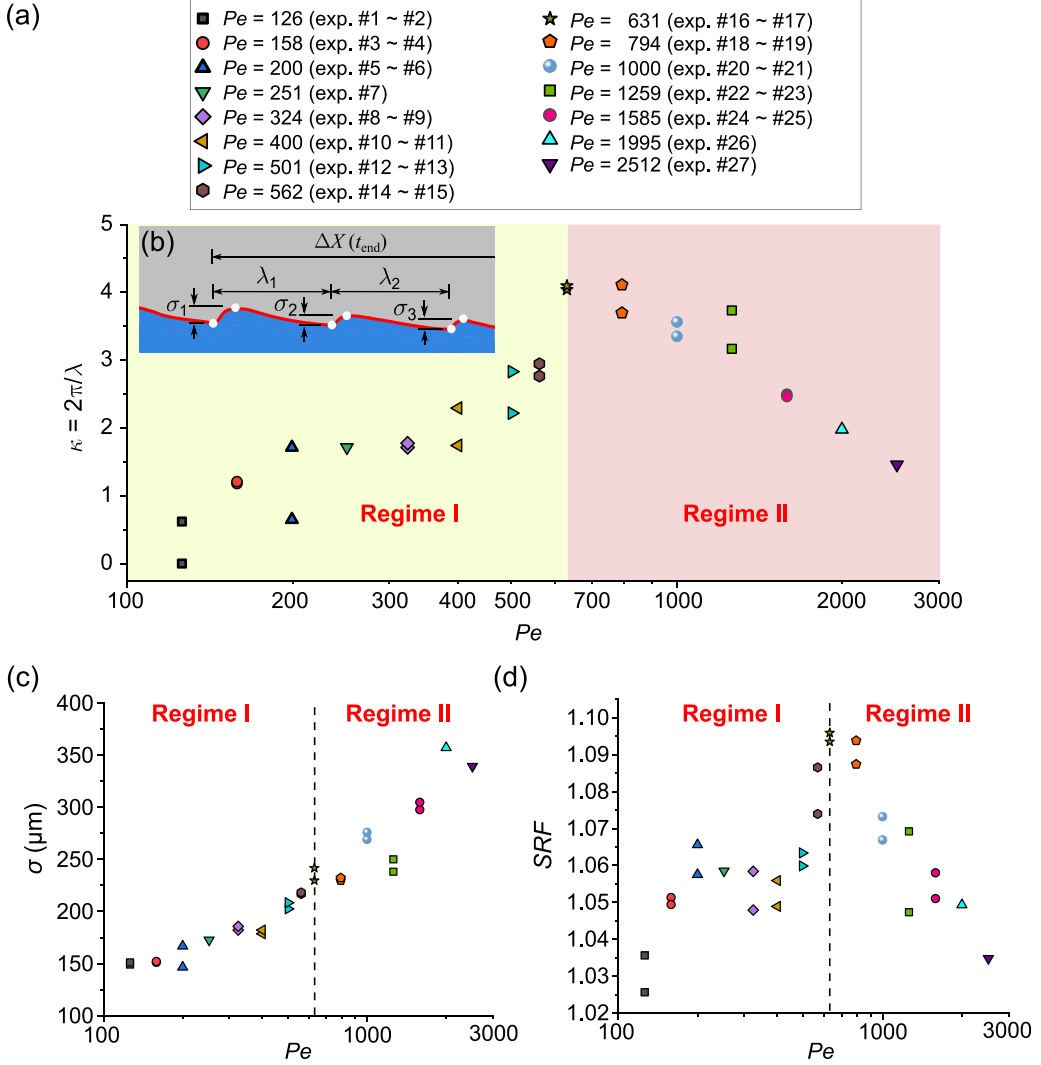


FIG. 7. Characterization of dissolution regimes. (a) Variation of average wave number  $\kappa$  vs  $Pe$  ( $t = t_{\text{end}}$ ). Two dissolution regimes are distinguished. At low flow rates, the wave number increases with the flow rate in Regime I. In Regime II, the wave number is reduced by increasing  $Pe$ . (b) Definition of the analyzed area and identifiable amplitudes ( $\sigma_1$ ,  $\sigma_2$ , and  $\sigma_3$ ) for  $Pe = 1995$ . Waves with amplitudes  $\sigma > \sim 150 \mu\text{m}$  are considered in the calculation. (c) Variation of the average amplitude of troughs  $\sigma$  vs  $Pe$  ( $t = t_{\text{end}}$ ). (d) Variation of the surface roughness factor (SRF) vs  $Pe$  ( $t = t_{\text{end}}$ ).

in MATLAB where the critical amplitude  $\sigma = \sim 150 \mu\text{m}$  is selected for peak identification [2,13] of the upper surface, and the average amplitude  $\sigma$  is computed as the average vertical distance between the apex of troughs and the upstream sharp tips [e.g.,  $\sigma_1$ ,  $\sigma_2$ , and  $\sigma_3$  in Fig. 7(b)]. The SRF is defined as the ratio between the total upper surface area ( $A_{\text{total}} = L_{\text{upper}}d_0$ ) and the geometric surface area ( $A_{\text{geo}} = Ld_0$ ), and it is calculated as  $\text{SRF} = A_{\text{total}}/A_{\text{geo}} = \frac{1}{L} \int_0^L \sqrt{1 + [y(x)]^2} dx$  [46,47], where  $y(x)$  denotes the roughness function of the upper surface. A larger  $\kappa$  indicates a surface sculptured by more convective plumes, that is, a more intensive effect of buoyancy-driven convection. [13,26]. From Fig. 7(a), we see that  $\kappa$  increases with  $Pe$  in Regime I ( $Pe = 126\text{--}631$ ), indicating that the

intensity of buoyancy-driven convection is enhanced by promoting the renewal of inflowing fluid. This is because the accelerated renewal of inflowing fresh water would generate a more prominent density difference near the upper surface by more rapidly transporting the dissolved salt away from the surface [34,35,42,44,48]. In addition, the average amplitude  $\sigma$  and the SRF both continually increase with  $Pe$  in Regime I [Figs. 7(c) and 7(d)], indicating a larger size of the trough in the vertical direction and a rougher surface for a larger flow rate. In Regime II, although the average amplitude  $\sigma$  increases with  $Pe$ ,  $\kappa$  and SRF both decrease. The decline of  $\kappa$  and SRF in this regime suggests a smoother solid surface with fewer troughs for a higher flow rate. The reason is that a larger horizontal flow rate would suppress the buoyancy-driven convection by driving less and wider convective plumes [20,22,31,32,49]. In conclusion, the dissolution regimes are greatly affected by the trough evolution. The underlying mechanism of trough evolution will be discussed in the following subsection.

Here, we further discuss the observed two regimes. According to Hu *et al.* [35], three dissolution regimes are observed in the 3D fracture under the gravity effect. Although the dissolution proceeds at different scales and dimensions, the regimes in their work are controlled by the interplay between buoyancy-driven and forced convections. They used the Richardson number  $Ri = \frac{\mu_f}{2\sqrt{3}D_m\rho_0} \cdot \frac{Ra}{Pe^2}$  (Rayleigh number  $Ra = \frac{\Delta\rho gb_0^3}{\mu_f D_m}$ ) to quantify the relative effect of natural convection and forced convection. From the natural to the forced convection regime, as  $Ri$  decreases, grooves are observed in the traverse direction, and the number of grooves increases from the natural to the mixed convection regime and then decreases from the mixed to the forced convection regime, like our observations. Likewise, we calculated  $Ri$ , which corresponds to the transition of regimes ( $Pe = 562\text{--}794$ ), in this paper. The critical  $Ri$  is calculated as  $Ri \approx 44\text{--}86$ , closely aligning with the transition ( $Ri \sim 10$ ) between the mixed and forced convection regimes in the work of Hu *et al.* [35]. This agreement manifests that the dissolution Regimes I and II observed in experiments are closely related to the interplay between buoyancy-driven and forced convections.

## B. Dissolution regimes controlled by eddies

To gain insights into the dissolution Regimes I and II observed in Figs. 6 and 7, we perform micro-PIV measurements near the trough position (Fig. 8). Interestingly, we observe that the evolution of the unstable solid-liquid interface is closely related to the developments of eddies at the local scale. From  $t = 8$  to 15 min, we observe the development of an eddy [Fig. 8(b) and Movie S1 in the Supplemental Material [43]] near the initial trough. During this period, the local dissolution rate, specifically the rate of local interface recession at the trough, experiences a notable acceleration [Fig. 8(a)]. However, from  $t = 15$  to 19 min, the area of the trough diminishes, and the eddy gradually dissipates [Fig. 8(b)]. The local dissolution rate becomes suppressed [Fig. 8(a)]. This implies that both the local dissolution rate and the area of trough are closely related to the eddy evolution. There exists a flow-dissolution feedback loop that controls the evolution of the channel geometry. To compare the relative effect of reaction to diffusion [11,13,42] involved in the system, we calculate the second Damköhler number  $Da_{II} = k_s(b_0)/D_m$ , where  $k_s$  is the reaction rate constant with  $k_s = 5 \times 10^{-4}$  m/s for dissolution of salt in water at 25 °C [11], and  $D_m = 1.61 \times 10^{-9}$  m<sup>2</sup>/s is the molecular diffusion coefficient [11]. We obtain that  $Da_{II}$  is  $\sim 155$ , showing that the dissolution is controlled by fast dissolution kinetics, as reported by previous authors [11,13]. Therefore, in the flow-dissolution system of this paper, the reaction is always limited by the diffusion, resulting in a nearly saturated CBL at the upper surface [11,13].

Based on the PIV measurement (Fig. 8), we present a conceptual description of the flow-dissolution feedback loop (Fig. 9) to show the role of eddies in dissolving the upper surface in a gravity field. When the first trough generates resulting from the buoyancy-driven convection, it provides a space for lighter fresh water to accumulate [Fig. 9(a)]; the concentration difference increases at this trough. Due to the nature of gravitational instability, a higher local dissolution rate is observed in the trough zone (see Movie S1 in the Supplemental Material [43]). As the flooding

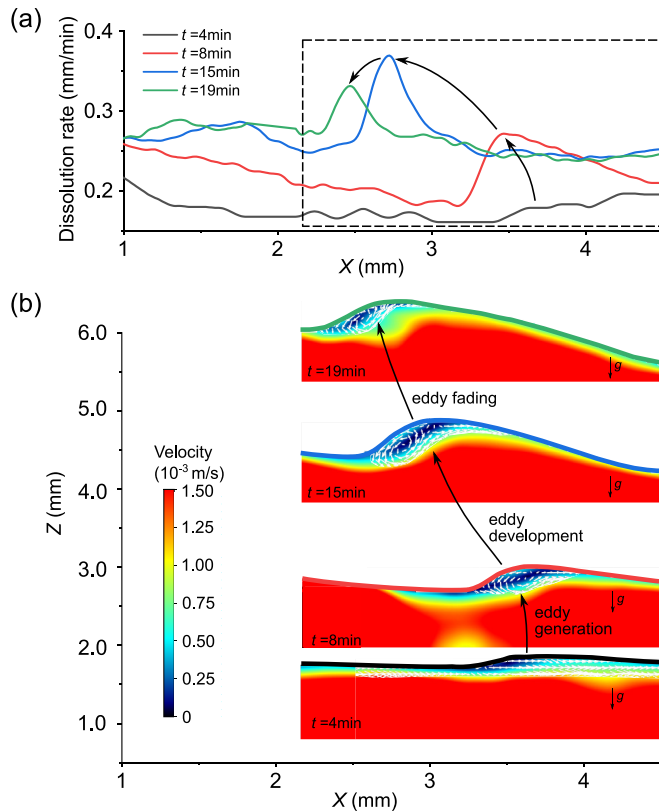


FIG. 8. Flow-dissolution feedback loop, characterized by the eddies at the pore scale, and its effect on local dissolution. (a) Evolution of local recession rate of the upper surface from  $t = 4$  to 19 min for  $Pe = 794$ . (b) Evolutions of upper surface geometry together with the flow velocity distribution at the location of the first trough for  $Pe = 794$  from  $t = 4$  to 19 min. The measured areas correspond to the dashed box location denoted in (a).

proceeds, the trough zone expands. Under the control of combined effects of buoyancy-driven and forced (mixed) convections, a counterclockwise eddy forms at the trough [Fig. 9(b)]. The dissolved salt can be quickly flushed away on the left side of the trough, promoting the local dissolution rate. From Figs. 9(a) to 9(b), the eddy generates due to the mixed convection, which involves the complex interplay among geometry evolution, flow, and dissolution. As the flooding further proceeds, the nonuniform local dissolution rate amplifies; that is, much more dissolution occurs on the left side. At the same time, the size of the trough increases, and the eddy develops. Such a development of the counterclockwise eddy would flush the dissolved salt from the top surface to the bottom on the left side [Fig. 9(c)]. This can be verified by the PIV measurement in Fig. 8 that the velocity on the left side of the trough is larger, and the local dissolution rate is also larger. The brine velocity acceleration by eddy during the dissolution process has also been reported in previous works [37–39]. As more and more of the solid phase is dissolved on the left side of the trough, the nonuniform local dissolution rate would smooth the upper surface, as depicted from Figs. 9(c) to 9(d). Here, this interplay between eddy and dissolution aligns with the findings of a significant study, where the eddy induces uneven dissolution near the solid surface due to the disparate flow velocity directions [38]. This eventually causes a decrease of the size of trough and further suppresses the development of the eddy (see Movie S3 in the Supplemental Material [43]). This conceptual model (Fig. 9), based on the PIV measurements, provides intuitive and clear understanding for the interplay

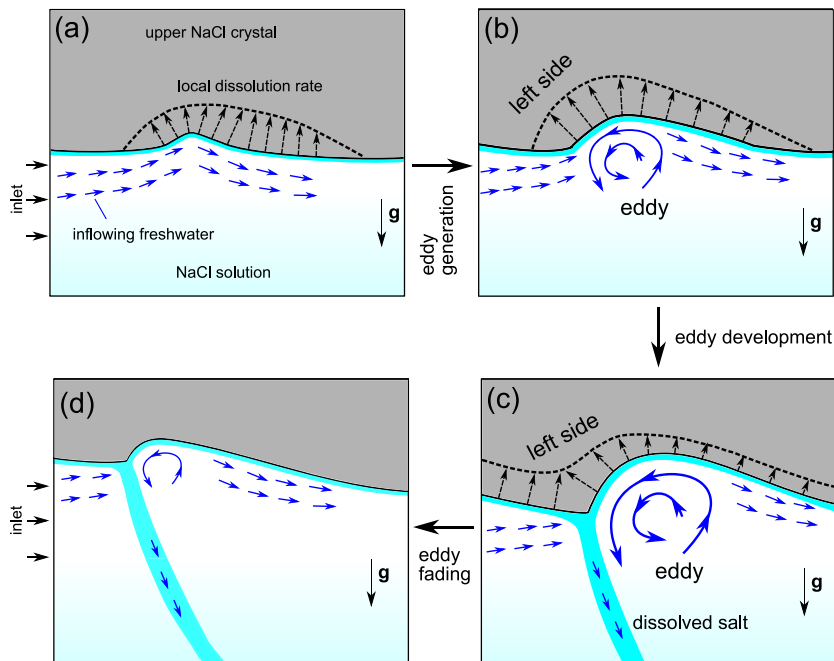


FIG. 9. Conceptual description of the flow-dissolution feedback loop associated with the eddy evolution in a gravity field. Due to the buoyancy-driven convection, the first trough occurs and provides a space for lighter fresh water to accumulate (a). As the flooding proceeds, the trough area expands, and a counterclockwise eddy forms at this trough (b). As the flooding further proceeds, the nonuniform local dissolution rate amplifies, and the counterclockwise eddy flushes the dissolved salt from the top surface to the bottom on the left side (c). As more and more solid phase is dissolved on the left side of the trough, the upper surface tends to be smooth (d).

among geometry evolution, flow, and dissolution. Although this interplay has been investigated via pore-scale simulation [37–39], the direct pore-scale experimental observation and quantification is not reported. We will further illustrate the effect of this flow-dissolution feedback loop on two dissolution regimes.

Here, we further discuss the generation of eddies in this system. The eddy generation here is in a gravity field where the effect of buoyancy cannot be neglected. Eddies can be observed even at low Pe cases of Regime I, and the plumes of denser dissolved salt can be seen at the ends of the troughs, namely, the crest positions between every two adjacent troughs, indicating that there is a continuous mass transfer between the eddy and the lower brine flow (see Movie S2 in the Supplemental Material [43]). To confirm the eddy is controlled by the mixed convection (combination of buoyancy-driven and forced convections), we then calculate the Reynolds number  $Re = \rho v \langle b \rangle / \mu$ , where  $v$  is the macroscopic fluid velocity, calculated by injection flow rate divided by channel cross-sectional area, i.e., arithmetic mean aperture times channel thickness,  $\langle b \rangle$  is the arithmetic mean aperture,  $\rho$  is the water density, and  $\mu$  is the water viscosity. For example, at  $Pe = 794$ ,  $Re$  near the first eddy position can be estimated as  $Re \sim 3$  at  $t = 844$  s, based on the actual flow rate near the upper surface. This value of  $Re$  is less than the critical value corresponding to eddy generation reported in the micron-scale fractured channel without buoyancy effect [48,50]. Considering that the eddy can also be observed even at lower Pe conditions ( $Pe = 324$  and  $400$  in Movie S2 in the Supplemental Material [43], for example), here, the eddy generation is concluded to be controlled by the effect of mixed convection.

Given that the eddies would etch troughs and control the local dissolution (Figs. 8 and 9), we now study how the eddies influence the dissolution regimes. We employ the number of troughs ( $n$ )

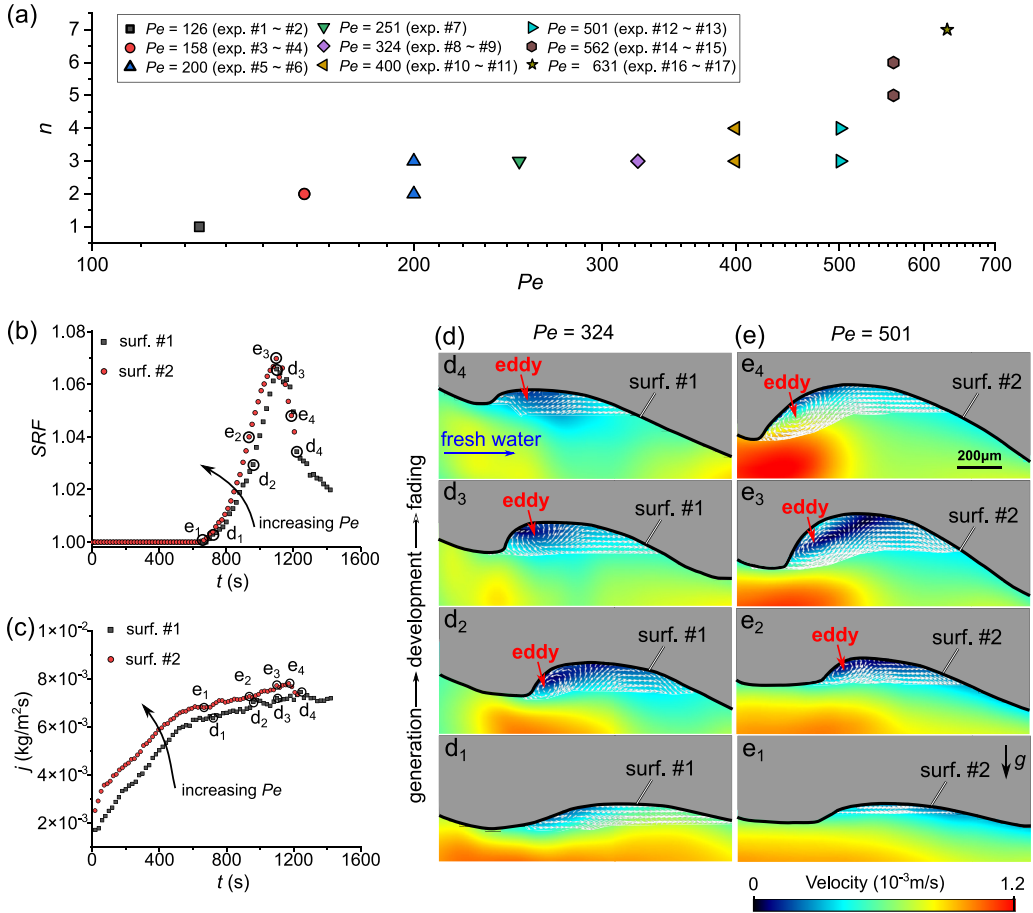


FIG. 10. The role of eddy evolution in Regime I. (a) Number of troughs on the upper surface at the sample scale in Regime I. (b) Temporal evolution of local surface roughness factor (SRF) for  $Pe = 324$  and  $501$ . (c) Temporal evolution of local mass transport current density ( $j$ ) for  $Pe = 324$  and  $501$ . (d) and (e) The local velocity field near surfs. #1 and #2 from eddy generation to fading. Locations of surfs. #1 and #2 are denoted by solid lines, and the eddies are also denoted. The colorbar from black to red shows the velocity magnitude.

on the upper surface, the local SRF, and local mass transport current density ( $j$ ) to characterize the effect of eddies in the two regimes. The local mass transport current density  $j$  signifies the intensity of local mass transfer, and it is defined as  $j = \Delta m / (A \Delta t)$  [25], where  $A = L_{\text{local}} d_0$  is defined as the area of the local surface ( $L_{\text{local}}$  is the length of local upper surface). It is important to note that, while  $A$  varies with time during dissolution, the variation during a short time step  $\Delta t$  is minimal. Consequently,  $A$  is recalculated at the beginning of each  $\Delta t$  ( $\sim 10$  s) time step. Here,  $\Delta m = \Delta V \rho_s$  is the mass of dissolved salt from this local surface during  $\Delta t$ , where  $\Delta V$  is the dissolved salt volumes during  $\Delta t$  and  $\rho_s = 2165 \text{ kg/cm}^3$  denotes the density of salt. The values for  $A$  and  $\Delta m$  can be determined based on a series of experimental images. In Regime I, the number of troughs  $n$  increases with  $Pe$  [Fig. 10(a)], showing that the effect of buoyancy-driven convection is promoted. It drives more convective plumes to create more troughs owing to the accelerated renewal of brine, as is discussed in Figs. 6 and 7 [11,42,44,48]. The evolution of the local roughness (SRF) and mass transport current density ( $j$ ) for the trough areas (surfs. #1 and #2) with time [Figs. 10(b) and 10(c)] suggests that the feedback loop (characterized by eddy evolution from generation, development

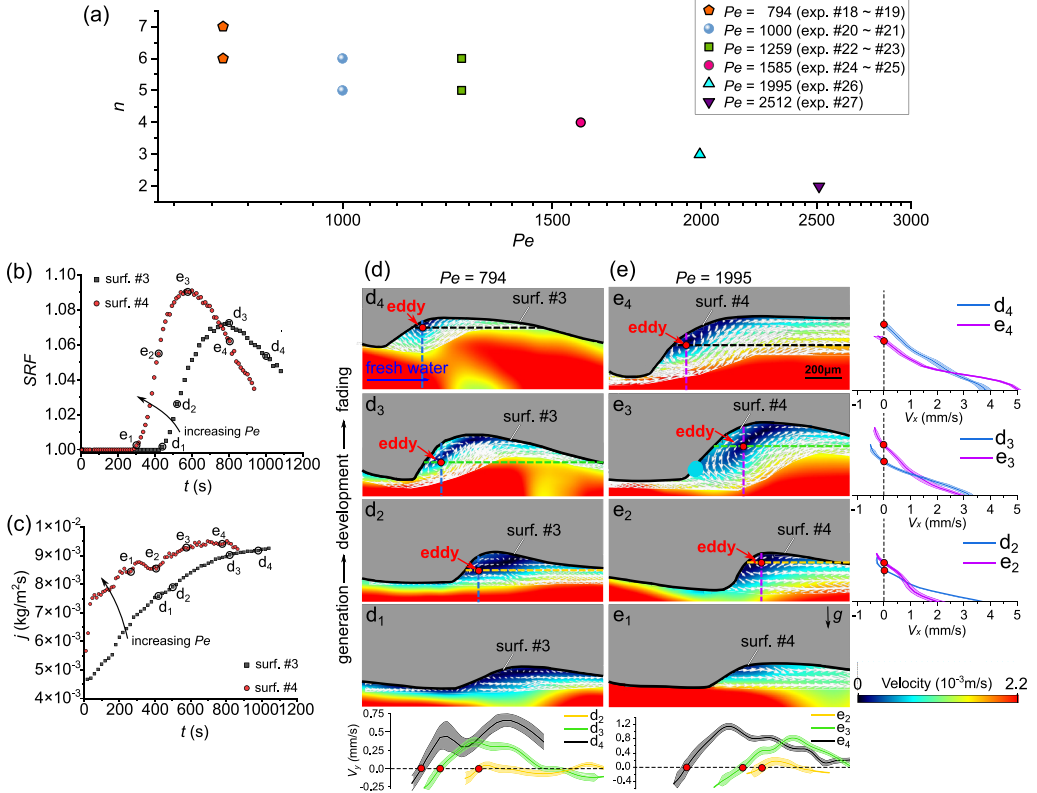


FIG. 11. The role of eddy evolution in Regime II. (a) Number of troughs on the upper surface at the sample scale in Regime II. (b) Temporal evolution of local surface roughness factor (SRF) for  $Pe = 794$  and 1995. (c) Temporal evolution of local mass transport current density ( $j$ ) for  $Pe = 794$  and 1995. (d) and (e) The local velocity field near surfs. #3 and #4 from eddy generation to fading. Locations of surfs. #3 and #4 are denoted by solid lines, and the eddies are also denoted. The colorbar from black to red shows the velocity magnitude. The rightmost column features horizontal velocity distribution curves for the profiles marked with red and blue vertical lines in surfs. #3 and #4. The bottom row displays vertical velocity distribution curves for the profiles marked with yellow, green, and black horizontal lines in surfs. #3 and #4. The red dots indicate the center positions of the eddies. The width of the shaded areas represents  $\pm$  standard deviation.

to fading) controls local interface evolution. The selected areas (surfs. #1 and #2) have equal size in the horizontal direction ( $\sim 2$  mm). The SRF of surfs. #1 and #2 increases during both the eddy generation and development [Figs. 10(d<sub>1</sub>)-10(d<sub>3</sub>) and 10(e<sub>1</sub>)-10(e<sub>3</sub>)] and decreases during the fading period [Figs. 10(d<sub>3</sub>)-10(b<sub>4</sub>) and 10(e<sub>1</sub>)-10(e<sub>3</sub>)]. The underlying mechanism is illustrated in Fig. 9, that is, the size of the trough gradually increases from generation to the development period, but then it shrinks as the eddy fades, resulting in a decrease in SRF. In addition, the mass transport current density  $j$  grows steadily during the whole period [Fig. 10(c)]. A larger  $j$  is observed for a higher  $Pe$ , characterized by the larger size of eddy [Figs. 10(d<sub>1</sub>)-10(d<sub>4</sub>) and 10(e<sub>1</sub>)-10(e<sub>4</sub>)], indicating the enhancing effect of  $Pe$  on the mass transport at the trough.

In Regime II, we observe results like Regime I for the SRF and  $j$  on the surfs. #3 and #4 at the local scale. The SRF increases at the stages of eddy generation and development and decreases at the fading stage. The mass transport current density  $j$ , again, grows steadily during the whole period [Fig. 11(c)]. These similar results indicate that the dissolution and mass transfer rates are enhanced by forced convection (a larger  $Pe$ ) at the local scale (at the scale of trough). However,

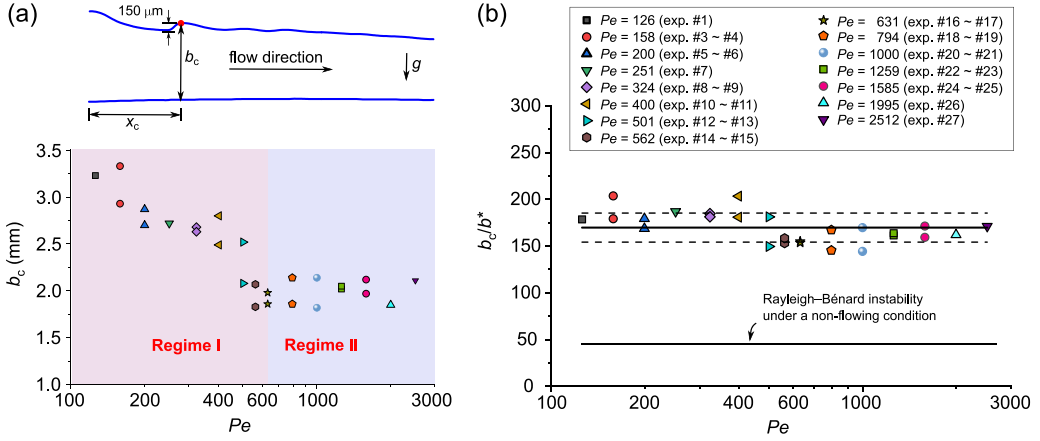


FIG. 12. The critical aperture for the onset of instability of solid-liquid surface. (a) Variation of  $b_c$  vs  $Pe$ . The schematic diagram shows the critical state when the first observable trough occurs. (b) The scaled aperture  $b_c/b^*$  for all experimental conditions shows a constant prefactor being  $\alpha_0 = 170 \pm 15$  for both dissolution Regimes I and II  $Pe$  after being modified. However, under a nonflowing condition, such a prefactor is  $\sim 50$ , highlighting the significant effect of forced convection.

the number of the trough decreases with  $Pe$  in Regime II, contrary to Regime I. The decline of the trough numbers suggests that the convective plumes driven by buoyancy-driven convection are diminished by the forced convection at the sample scale in the Regime II, which is also evidenced by Figs. 7(a) and 7(d). To further quantify the eddies, we select velocity distribution profiles at certain cross-sections passing through the eddy center (marked with red dots where  $V_x = V_y = 0$ ). We calculated the horizontal velocity ( $V_x$ ) distribution along vertical cross-section positions (indicated in blue and purple) and the vertical velocity ( $V_y$ ) distribution along horizontal cross-section positions (marked in black, green, and yellow). The width of the shaded areas represents  $\pm$  standard deviation. The distribution of  $V_x$  along the vertical cross-section at the eddy center indicates that, under the effect of the eddy,  $V_x$  near the top of the trough increases as eddy generates and develops, followed by a decrease in eddy fading period [Figs. 11(d<sub>2</sub>)-11(d<sub>4</sub>) and 11(e<sub>2</sub>)-11(e<sub>4</sub>)]. Additionally, the distribution of  $V_y$  along the horizontal cross-section elucidates that, as dissolution proceeds, the  $V_y$  near the left side of the trough initially increases and then stabilizes. The observed distributions of  $V_x$  and  $V_y$  here have the potential to explain the evolution of the trough during the eddy fading period shown in Fig. 9.

### C. Onset of the solid-liquid instability

As previously indicated, the solid-liquid interface is smooth initially and then becomes rough with troughs induced by eddies, as shown in Fig. 6. It implies that there exists a critical state that the solid-liquid interface transits from stable to unstable. From the experimental observation, such a transition corresponds to the first trough etched at the surface [Fig. 12(a)]. In this subsection, we study the critical aperture  $b_c$  at which the first trough occurs. We first present the variation of the critical aperture  $b_c$ . As shown in Fig. 12(a), the critical aperture  $b_c$  decreases with  $Pe$  in Regime I but reaches a plateau in Regime II. This is because this critical aperture  $b_c$  depends on density difference  $\Delta\rho$  in our experiments. As previously reported, this critical aperture  $b_c$  scales with a characteristic length  $b^*$  [51], such as

$$b_c \sim b^* = \left( \frac{\mu_f D_m}{g \Delta \rho} \right)^{1/3}, \quad (1)$$

in which all the parameters are given in our experiments except for the density difference  $\Delta\rho$ . In the dissolution Regime I, the renewal of brine driven by forced convection is considered so weak that the local density difference near the upper surface  $\Delta\rho$  is expected to be significantly lower than the maximum one ( $\Delta\rho_m = 200 \text{ kg/m}^3$ ) [34,42]. Consequently, the critical aperture  $b_c$  is larger at a lower flow-rate condition. As expected [Fig. 12(a)], as the flow rate increases in Regime I, the local density difference  $\Delta\rho$  increases, causing the critical aperture to decrease and further approach a plateau at Regime II.

To gain insights into the critical aperture under various flow-rate conditions, we first estimate the local density difference  $\Delta\rho$  involved in  $b^*$ . To do so, we estimate the mass concentration  $C(x_c)$  at the first trough position ( $x = x_c$ ) using the analytical solution reported by Szymczak and Ladd [52,53] (see Appendix A for more details):

$$C(x_c) = C_{\text{sat}} - (C_{\text{sat}} - C_{\text{in}}) \exp\left(\frac{-x_c 2k_{\text{eff}}}{q}\right), \quad (2)$$

$$k_{\text{eff}}(h) = \frac{k}{1 + 2kh/D_m \text{Sh}}. \quad (3)$$

In Eq. (2), the position for the first trough  $x_c$  can be directly measured, as listed in Table I;  $C_{\text{sat}}$  is the saturation mass concentration calculated as  $C_{\text{sat}} = \rho_{\text{sat}}\omega_{\text{sat}} = 312 \text{ g/L}$ , where  $\rho_{\text{sat}}$  is the density of saturated sodium chloride solution ( $\rho_{\text{sat}} = 1200 \text{ kg/m}^3$ ),  $\omega_{\text{sat}}$  is the mass fraction of NaCl in saturated sodium chloride solution at  $25^\circ\text{C}$  ( $\omega_{\text{sat}} = 0.26$ ),  $C_{\text{in}} = 0$  is the inflow concentration (fresh water), and  $q$  is the volume flow rate per unit width  $q = Q/T$ . In Eq. (3),  $k_{\text{eff}}$  is the effective reaction rate which depends on the reaction rate constant  $k$  for NaCl crystal ( $k = 5 \times 10^{-4} \text{ m/s}$  for dissolution of salt in water at  $25^\circ\text{C}$  [54]), the aperture of channel  $h$ , the molecular diffusion coefficient  $D_m$ , and the Sherwood number  $\text{Sh}$  (see more details in Appendix A). After the concentration is obtained by Eq. (2), the density difference  $\Delta\rho$  can also be determined by the density-concentration relationship [11,13,55], such as  $\Delta\rho(x_c) = \Delta\rho_m(1 - C(x_c)/C_{\text{sat}})$ . Substituting this equation into Eq. (1), we obtain a relationship for the critical capture  $b_c$ :

$$b_c = \alpha_0 \left[ \frac{\mu_f D_m}{g \Delta\rho(x_c)} \right]^{1/3}. \quad (4)$$

By Eq. (4), Fig. 12(b) shows the variation of the scaled  $b_c$ , that is,  $b_c / \{\mu_f D_m / [g \Delta\rho(x_c)]\}^{1/3}$ , with  $\text{Pe}$ . We obtain a constant prefactor of  $\alpha_0 = 170 \pm 15$  for both dissolution Regimes I and II. The rescaled value of  $b_c/b^*$  varies within 10%, indicating the reasonability of this rescaling for both regimes. The obtained constant prefactor in both regimes indicates that  $b_c$  is determined by a competition between buoyancy ( $g\Delta\rho$ ) and the stabilizing effects of viscosity ( $\mu_f$ ) and mass diffusion ( $D_m$ ). This rescaling has been confirmed to be applicable for various cases, including fluid pairs with different viscosities and density differences [51]. Without an external-flowing condition in a horizontal fracture, such a prefactor is  $\sim 50$ , much lower than that of this paper [51]. This is because the onset of the instability here corresponds to the deformation of the solid-liquid interface involving a moving, deformable solid boundary [25]. However, the previous work focused on the onset of the buoyancy-driven convection cell (such as a mushroomlike structure) when the evolution of the solid surface has not been affected yet. Further, Eq. (4) considers the effects of the forced convection in dissolving the channel, while a larger number of the previous works focused on the pure natural convection system (without external-flowing condition).

#### IV. CONCLUSIONS

We visualize and quantify the transition of dissolution regimes of a horizontal channel in a gravity field. We show that the dissolution shifts from Regime I to II as  $\text{Pe}$  increases. The flow-dissolution feedback loop, associated with the eddy evolution is revealed by micro-PIV imaging, characterized by the eddy generation, development to fading. We further investigate the effect of eddy evolution



on the two regimes, suggesting that the buoyancy-driven convection is reduced in Regime II and enhanced in Regime I by the forced convection. Finally, we obtain a critical aperture for the onset of instability of the solid-liquid interface and approach a constant prefactor of  $\alpha_0 = b_c/b^* = 170 \pm 15$  for both dissolution regimes. In this paper, we develop a flow-visualization approach to investigate the flow-dissolution feedback in a gravity field. We also improve our understanding of how the interplay between buoyancy-driven and forced convections reshapes the solid surface during dissolution.

### ACKNOWLEDGMENTS

We acknowledge support from the National Natural Science Foundation of China (No. 52122905 and No. 51925906), the Basic Science Center Program for Multiphase Media Evolution in Hypergravity of the National Natural Science Foundation of China (No. 51988101), and the Fundamental Research Funds for the Central Universities (No. 2042023kfyq03).

### APPENDIX A: THE CALCULATION OF $C(x_c)$ USING EQ. (2)

In the case of a single fracture, similar geometry to this study,  $C(x)$  along the flow path can be described by Eq. (2), as reported in Refs. [52,53]. In this equation,  $Sh$  is the Sherwood number, which depends on the reaction rate at the surfaces, but the variation is relatively small in the range of 7.54 [high reaction rates (transport limit)]  $\sim$  8.24 [low reaction rates (reaction limit)]. Here, we approximate the Sherwood number by a constant value  $Sh = 8$  [53]. Regarding the values of  $h$  and  $k$  in Eq. (3), given that freshwater always flows near the upper surface due to the buoyancy effect, its distribution is observed to be little affected by the dissolution. As an approximation, we employ the values of the initial state ( $h = \langle b_0 \rangle$ ) and  $q = Q_{inj}/d_0$ ) involved in Eqs. (2) and (3) to estimate the concentration at the first observable trough  $C(x_c)$ . As the position of the first observable trough ( $x = x_c$ , in Table I) and its corresponding aperture ( $b_c$ ) can be directly measured through the experiments [Fig. 12(a)], the concentration at the first trough position [ $C(x_c)$ ] can be obtained via Eqs. (2) and (3). Given the density difference is usually considered linear with concentration difference [11,13,55], we can then obtain  $\Delta\rho(x_c)$  and scale the characteristic length  $b^*$  for various  $Pe$ 's.

### APPENDIX B: DETAILS OF THE FLOW-THROUGH EXPERIMENTS

Figure 2 shows the detailed configuration of the micro-PIV system used in this paper. Figure 5 shows the displacement of saturated brine by fresh water [Figs. 5(a) and 5(b)] and the solid dissolution due to continuous flooding of fresh water [Figs. 5(b) and 5(c)]. Before the beginning of dissolution, the channel is filled with saturated brine [Fig. 5(a)]. As we start the infuse mode of the syringe pump, the freshwater, dyed with Erioglaucine disodium salt (Macklin, E808678), gradually flows into the channel to displace the saturated brine. The solid-liquid interface remains stationary until the channel is nearly filled with dyed freshwater [Fig. 5(b)]. The solid-liquid interface dissolution, shown by the recession of channel interfaces, is then observed [Fig. 5(c)], suggesting no dissolution in the displacement process [Figs. 5(a) and 5(b)]. The state [Fig. 5(b)] of the beginning of the recession of channel interfaces is defined as the beginning of dissolution ( $t = 0$  s).

### APPENDIX C: FLOW VELOCITY DISTRIBUTION IN CHANNEL

To investigate the distribution of flow velocity within the channel, we conducted PIV measurements during the dissolution processes, as depicted in Fig. 13. It shows that the flow velocity near the upper surface is significantly higher than that at the bottom. This is because the buoyancy effect causes lighter fresh water to preferentially flow near the upper surface. The lower region, characterized by a lower flow rate, seems to contain a higher concentration of denser dissolved salt. This would reduce the mass transfer, suppressing the solid dissolution at the bottom surface

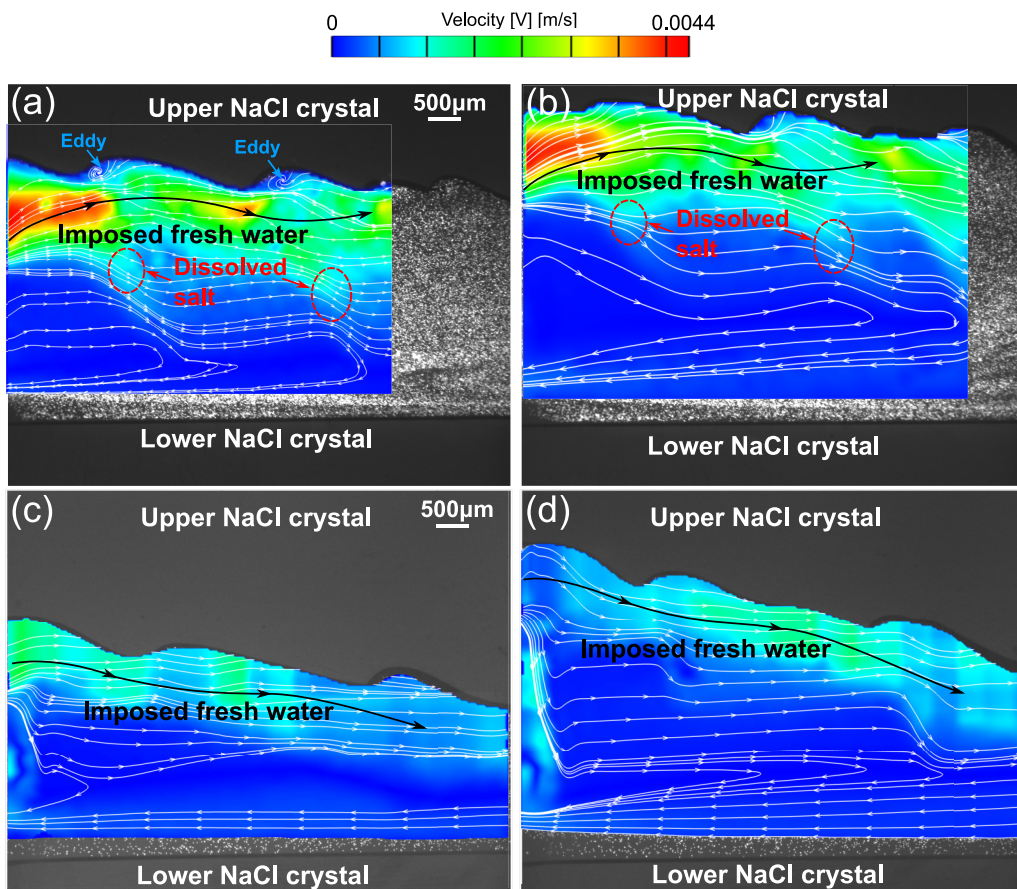


FIG. 13. The distribution of the flow velocity field in the channel. (a) Flow velocity field for  $Pe = 794$  at  $t = 900$  s. (b) Flow velocity field for  $Pe = 794$  at  $t = 1080$  s. (c) Flow velocity field for  $Pe = 324$  at  $t = 840$  s. (d) Flow velocity field for  $Pe = 324$  at  $t = 1200$  s. The colors correspond to the velocity magnitude.

(as shown in Movie S2 in the Supplemental Material [43]). Moreover, the flow rate near the upper surface appears to be minimally influenced by channel expansion during dissolution, primarily due to the preferentially flow induced by buoyancy effect [as evident in Figs. 13(a) and 13(b) for Regime II]. Similar results are also observed in Regime I [Figs. 13(c) and 13(d)].

- 
- [1] P. Meakin and B. Jamtveit, Geological pattern formation by growth and dissolution in aqueous systems, *Proc. R. Soc. A* **466**, 659 (2010).
  - [2] A. Guérin, J. Derr, S. Courrech du Pont, and M. Berhanu, Streamwise dissolution patterns created by a flowing water film, *Phys. Rev. Lett.* **125**, 194502 (2020).
  - [3] P. Szymczak, From slots to tubes: The influence of dimensionality on fracture dissolution models, *Acta Geophys.* **61**, 1556 (2013).
  - [4] J. K. Warren, *Evaporites: A Geological Compendium* (Springer, Cham, 2016).
  - [5] S. Mojtaba, R. Behzad, N. M. Rasoul, and R. Mohammad, Experimental study of density-driven convection effects on  $\text{CO}_2$  dissolution rate in formation water for geological storage, *J. Nat. Gas Sci. Eng.* **21**, 600 (2014).

- [6] R. Nazari Moghaddam, B. Rostami, and P. Pourafshary, Scaling analysis of the convective mixing in porous media for geological storage of CO<sub>2</sub>: An experimental approach, *Chem. Eng. Commun.* **202**, 815 (2015).
- [7] J. J. Hidalgo, C. W. MacMinn, and R. Juanes, Dynamics of convective dissolution from a migrating current of carbon dioxide, *Adv. Water Resour.* **62**, 511 (2013).
- [8] H. Fazeli, M. Nooraiepour, and H. Hellevang, Microfluidic study of fracture dissolution in carbonate-rich caprocks subjected to CO<sub>2</sub>-charged brine, *Ind. Eng. Chem. Res.* **59**, 450 (2020).
- [9] S. Wang, Z. Cheng, Y. Zhang, L. Jiang, Y. Liu, and Y. Song, Unstable density-driven convection of CO<sub>2</sub> in homogeneous and heterogeneous porous media with implications for deep saline aquifers, *Water Resour. Res.* **57**, e2020WR028132 (2021).
- [10] M. H. Doranehgard and H. Dehghanpour, Quantification of convective and diffusive transport during CO<sub>2</sub> dissolution in oil: A numerical and analytical study, *Phys. Fluids* **32**, 085110 (2020).
- [11] J. Philippi, M. Berhanu, J. Derr, and S. Courrech du Pont, Solutal convection induced by dissolution, *Phys. Rev. Fluids* **4**, 103801 (2019).
- [12] M. Berhanu, J. Philippi, S. Courrech du Pont, and J. Derr, Solutal convection instability caused by dissolution, *Phys. Fluids* **33**, 076604 (2021).
- [13] C. Cohen, M. Berhanu, J. Derr, and S. Courrech du Pont, Buoyancy-driven dissolution of inclined blocks: Erosion rate and pattern formation, *Phys. Rev. Fluids* **5**, 053802 (2020).
- [14] M. S. Davies Wykes, J. M. Huang, G. A. Hajjar, and L. Ristroph, Self-sculpting of a dissolvable body due to gravitational convection, *Phys. Rev. Fluids* **3**, 043801 (2018).
- [15] M. T. Elenius, D. V. Voskov, and H. A. Tchelepi, Interactions between gravity currents and convective dissolution, *Adv. Water Resour.* **83**, 77 (2015).
- [16] J. A. Neufeld, M. A. Hesse, A. Riaz, M. A. Hallworth, H. A. Tchelepi, and H. E. Huppert, Convective dissolution of carbon dioxide in saline aquifers: Convective dissolution of carbon dioxide, *Geophys. Res. Lett.* **37**, L22404 (2010).
- [17] B. Favier, J. Purseed, and L. Duchemin, Rayleigh-Bénard convection with a melting boundary, *J. Fluid Mech.* **858**, 437 (2019).
- [18] J. J. Hidalgo and J. Carrera, Effect of dispersion on the onset of convection during CO<sub>2</sub> sequestration, *J. Fluid Mech.* **640**, 441 (2009).
- [19] R. Guo, H. Sun, Q. Zhao, Z. Li, Y. Liu, and C. Chen, A novel experimental study on density-driven instability and convective dissolution in porous media, *Geophys. Res. Lett.* **48**, e2021GL095619 (2021).
- [20] S. Mahmoodpour, B. Rostami, M. R. Soltanian, and M. A. Amooie, Convective dissolution of carbon dioxide in deep saline aquifers: Insights from engineering a high-pressure porous visual cell, *Phys. Rev. Appl.* **12**, 034016 (2019).
- [21] P. J. Kreyenberg, H. H. Bauser, and K. Roth, Velocity field estimation on density-driven solute transport with a convolutional neural network, *Water Resour. Res.* **55**, 7275 (2019).
- [22] H. Emami-Meybodi, H. Hassanzadeh, and J. Ennis-King, CO<sub>2</sub> dissolution in the presence of background flow of deep saline aquifers, *Water Resour. Res.* **51**, 2595 (2015).
- [23] A. Riaz and Y. Cinar, Carbon dioxide sequestration in saline formations: Part I—Review of the modeling of solubility trapping, *J. Petrol. Sci. Eng.* **124**, 367 (2014).
- [24] S. S. Gopalakrishnan, J. Carballido-Landeira, A. De Wit, and B. Knaepen, Relative role of convective and diffusive mixing in the miscible Rayleigh-Taylor instability in porous media, *Phys. Rev. Fluids* **2**, 012501(R) (2017).
- [25] T. S. Sullivan, Y. Liu, and R. E. Ecke, Turbulent solutal convection and surface patterning in solid dissolution, *Phys. Rev. E* **54**, 486 (1996).
- [26] C. Cohen, M. Berhanu, J. Derr, and S. Courrech du Pont, Erosion patterns on dissolving and melting bodies, *Phys. Rev. Fluids* **1**, 050508 (2016).
- [27] J. J. Hidalgo, M. Dentz, Y. Cabeza, and J. Carrera, Dissolution patterns and mixing dynamics in unstable reactive flow: Mixing in unstable reactive flow, *Geophys. Res. Lett.* **42**, 6357 (2015).
- [28] H. Luo, M. Quintard, G. Debenest, and F. Laouafa, Properties of a diffuse interface model based on a porous medium theory for solid-liquid dissolution problems, *Comput. Geosci.* **16**, 913 (2012).

- [29] H. Emami-Meybodi, H. Hassanzadeh, C. P. Green, and J. Ennis-King, Convective dissolution of CO<sub>2</sub> in saline aquifers: Progress in modeling and experiments, *Int. J. Greenh. Gas Con.* **40**, 238 (2015).
- [30] H. Emami-Meybodi, Dispersion-driven instability of mixed convective flow in porous media, *Phys. Fluids* **29**, 094102 (2017).
- [31] A. Tsinober, R. Rosenzweig, H. Class, R. Helmig, and U. Shavit, The role of mixed convection and hydrodynamic dispersion during CO<sub>2</sub> dissolution in saline aquifers: A numerical study, *Water Resour. Res.* **58**, e2021WR030494 (2022).
- [32] I. Michel-Meyer, U. Shavit, A. Tsinober, and R. Rosenzweig, The role of water flow and dispersive fluxes in the dissolution of CO<sub>2</sub> in deep saline aquifers, *Water Resour. Res.* **56**, e2020WR028184 (2020).
- [33] P. E. Dijk and B. Berkowitz, Buoyancy-driven dissolution enhancement in rock fractures, *Geology* **28**, 1051 (2000).
- [34] R. Hu, T. Wang, Z. Yang, Y. Xiao, Y. Chen, and C. Zhou, Dissolution hotspots in fractures, *Geophys. Res. Lett.* **48**, e2021GL094118 (2021).
- [35] R. Hu, K. Li, C. Zhou, T. Wang, Z. Yang, and Y. Chen, On the role of gravity in dissolving horizontal fractures, *J. Geophys. Res. Solid Earth* **128**, e2022JB025214 (2023).
- [36] A. W. A. Ahoulou, A.-J. Tinet, C. Oltéan, and F. Golfier, Experimental insights into the interplay between buoyancy, convection, and dissolution reaction, *J. Geophys. Res. Solid Earth* **125**, e2020JB020854 (2020).
- [37] J. Yang, H. Li, C. Yang, Y. Li, T. Wang, X. Shi, and Y. Han, Physical simulation of flow field and construction process of horizontal salt cavern for natural gas storage, *J. Nat. Gas Sci. Eng.* **82**, 103527 (2020).
- [38] L. Li, R. Gracie, M. B. Dusseault, N. Xiao, and W. Liang, Modeling and verification of non-linear mineral dissolution processes with buoyancy effects, *Int. J. Rock Mech. Min. Sci.* **161**, 105257 (2023).
- [39] L. Li, E. Rivas, R. Gracie, and M. B. Dusseault, Methodology for the nonlinear coupled multi-physics simulation of mineral dissolution, *Int. J. Numer. Anal. Meth. Geomech.* **45**, 2193 (2021).
- [40] F. Kazemifar, G. Blois, M. Aybar, P. Perez Calleja, R. Nerenberg, S. Sinha, R. J. Hardy, J. Best, G. H. Sambrook Smith, and K. T. Christensen, The effect of biofilms on turbulent flow over permeable beds, *Water Resour. Res.* **57**, e2019WR026032 (2021).
- [41] F. Kazemifar, G. Blois, D. C. Kyritsis, and K. T. Christensen, A methodology for velocity field measurement in multiphase high-pressure flow of CO<sub>2</sub> and water in micromodels, *Water Resour. Res.* **51**, 3017 (2015).
- [42] C. Zhou, R. Hu, H. Li, Z. Yang, and Y. Chen, Pore-scale visualization and quantification of dissolution in microfluidic rough channels, *Water Resour. Res.* **58**, e2022WR032255 (2022).
- [43] See Supplemental Material at <http://link.aps.org/supplemental/10.1103/PhysRevFluids.8.123902> for Movie S1 illustrating the development of eddies, Movie S2 showing the trajectory of particles throughout the channel, and Movie S3 depicting the eddy fading processes.
- [44] T. Wang, R. Hu, Z. Yang, C. Zhou, Y. Chen, and C. Zhou, Transitions of dissolution patterns in rough fractures, *Water Resour. Res.* **58**, e2021WR030456 (2022).
- [45] R. C. Kerr, Convective crystal dissolution, *Contrib. Mineral. Petr.* **121**, 237 (1995).
- [46] J. You and K. J. Lee, A pore-scale investigation of surface roughness on the evolution of natural fractures during acid dissolution using DBS method, *J. Petrol. Sci. Eng.* **204**, 108728 (2021).
- [47] H. Deng, S. Molins, D. Trebotich, C. Steefel, and D. DePaolo, Pore-scale numerical investigation of the impacts of surface roughness: Upscaling of reaction rates in rough fractures, *Geochim. Cosmochim. Ac.* **239**, 374 (2018).
- [48] S. H. Lee, I. W. Yeo, K.-K. Lee, and W. S. Lee, The role of eddies in solute transport and recovery in rock fractures: Implication for groundwater remediation, *Hydrol. Process.* **31**, 3580 (2017).
- [49] S. K. Hansen, Y. Tao, and S. Karra, Impacts of permeability heterogeneity and background flow on supercritical CO<sub>2</sub> dissolution in the deep subsurface, *Water Resour. Res.* **59**, e2023WR035394 (2023).
- [50] S. H. Lee, I. W. Yeo, K.-K. Lee, and R. L. Detwiler, Tail shortening with developing eddies in a rough-walled rock fracture: Tail shortening with eddies in fractures, *Geophys. Res. Lett.* **42**, 6340 (2015).
- [51] S. Alqatari, T. E. Videbæk, S. R. Nagel, A. E. Hosoi, and I. Bischofberger, Confinement-induced stabilization of the Rayleigh-Taylor instability and transition to the unconfined limit, *Sci. Adv.* **6**, eabd6605 (2020).

- [52] P. Szymczak and A. J. C. Ladd, The initial stages of cave formation: Beyond the one-dimensional paradigm, [Earth Planet. Sc. Lett. \*\*301\*\*, 424 \(2011\)](#).
- [53] P. Szymczak and A. J. C. Ladd, Reactive-infiltration instabilities in rocks. fracture dissolution, [J. Fluid Mech. \*\*702\*\*, 239 \(2012\)](#).
- [54] L. A. Calcada, L. A. A. Martins, C. M. Scheid, S. C. Magalhães, and A. L. Martins, Mathematical model of dissolution of particles of nacl in well drilling: Determination of mass transfer convective coefficient, [J. Petrol. Sci. Eng. \*\*126\*\*, 97 \(2015\)](#).
- [55] C. Oltéan, F. Golfier, and M. A. Buès, Numerical and experimental investigation of buoyancy-driven dissolution in vertical fracture: Buoyancy-driven dissolution in fracture, [J. Geophys. Res. Solid Earth \*\*118\*\*, 2038 \(2013\)](#).